Chin. Sci. Bull. (2014) 59(8):785–794
DOI 10.1007/s11434-013-0101-9

csb.scichina.com
www.springer.com/scp

Article

Oceanology

Investigating different bio-responses of the upper ocean to Typhoon Haitang using Argo and satellite data

Haixia Shan · Yuping Guan · Jianping Huang

Received: 30 April 2013 / Accepted: 24 July 2013 / Published online: 23 January 2014

Abstract The responses of the upper ocean to Typhoon Haitang in July 2005 are investigated using Argo float and multiplatform satellite data. The results show decreasing sea surface temperature (SST), a deepening of the mixed layer depth (MLD), and enhanced Chlorophyll-*a* (Chl-*a*) concentration. Two extreme cool regions are identified. While the magnitude of SST cooling in the two regions is similar, the biological response (Chl-*a* enhancement) differs. To facilitate comparisons, the region to the northeast of Taiwan is defined as region A and the region east of Taiwan as region B. Ekman pumping and the intrusion of the Kuroshio play an important role in the enhancement of Chl-*a* in region A. Cold eddies provide the material source for the formation of the cold center in region B, where mixing is dominant. Because of the relatively high translation speed (5 m/s) in region B, Ekman pumping has little influence on the cooling and Chl-*a* enhancement processes. Moreover, the MLD is shallower than the nutricline, which means that mixing does not result in a marked increase in nutrients in the euphotic layer (where the nutrient concentration is uniformly depleted). Sea temperatures, in contrast, gradually decrease with depth below the bottom of the mixed layer. In contrast to region A, region B showed no significant enhancement of Chl-*a* but strong SST cooling.

Keywords Ocean response · Tropical cyclone · SST cooling · Ekman pumping · Chlorophyll-*a* enhancement

H. Shan · J. Huang
Key Laboratory for Semi-Arid Climate Change of the Ministry of Education, College of Atmospheric Sciences, Lanzhou University, Lanzhou 730000, China

H. Shan · Y. Guan (✉)
State Key Laboratory of Tropical Oceanography, South China Sea Institute of Oceanology, Chinese Academy of Sciences, Guangzhou 510301, China
e-mail: guan@scsio.ac.cn

1 Introduction

Tropical cyclones (TCs) can cause a significant decrease in sea surface temperature (SST) and enhanced Chlorophyll-*a* (Chl-*a*) concentration. Previous studies have shown that SST dropped by more than 9 and 11 °C in response to the passage of typhoons Kai-Tak [1] and Lingling [2], respectively. In addition, SST cooling of 2.0–2.5 °C has been also attributed to the equatorial typhoon Vamei, which formed at 1°30′N [3]. The primary mechanisms accounting for the cooling caused by TCs include entrainment/vertical mixing, upwelling, exchange of air–sea heat fluxes, and the intensity and translation speed of TCs [4–8]. The upper ocean cooling is mainly controlled by the entrainment of cold water from the thermocline into the mixed layer. The entrainment/mixing accounts for 75 %–90 % of the SST drop in the wake of a TC [4, 6, 7]. Upwelling can cause a significant SST cooling response to a slowly moving TC (<4 m/s) [4]. Ocean mixing and upwelling induced by the passage of a typhoon can bring the nutrient-rich water of the bottom layer to the euphotic layer, where light is abundant for photosynthesis but nutrients are commonly in short supply. These conditions contribute to the growth of phytoplankton and the enhancement of Chl-*a* concentrations at the ocean surface. Chl-*a* enhancement ranges from 5 % to 91 % in the wake of hurricanes [9], with elevated levels typically lasting

2–3 weeks before returning to pre-hurricane concentrations.

Recent studies of the upper ocean response to TCs emphasize the importance of understanding the dynamic processes and interactions with the atmosphere, ocean currents, wave breaking, and spray effects [10–15]. Oceanic responses to individual TCs are unique, which makes generalization of the processes problematic. There are many existing studies in relation to Typhoon Haitang [16–24]. For example, the impact of pre-existing oceanic conditions on predictions of a TC during its intensification phase has been evaluated by forcing a coupled atmosphere–ocean model with different initial oceanic conditions [21]. Wada et al. [22] investigated the wave–ocean interaction of Typhoon Haitang using a numerical model. Chang et al. [24] used satellite-tracked drifter data to study the surface flows in the Taiwan Strait during Typhoon Haitang's passage. Although the SST cold patch is usually a pronounced feature of a moving typhoon, the dynamic and thermodynamic processes associated with the SST cold patch during Typhoon Haitang remain poorly understood [16–19, 23]. Indeed, two distinct cold patches with similar magnitude have been identified associated with Haitang. Significant enhancement of Chl-*a* was found to the northeast of Taiwan, and the mechanisms accounting for the strong cooling and Chl-*a* enhancement have been investigated in a previous study [16]. However, there was no obvious enhancement of Chl-*a* in the east region of Taiwan. Indeed, Chl-*a* enhancement is usually accompanied by SST cooling after the passing of a typhoon, and an inverse correlation between SST and Chl-*a* concentration has been widely reported [1, 9, 25, 26]. Here we use various datasets to confirm the mechanisms (as proposed in previous studies) of the similar SST cooling in the two regions. In particular, we explore the possible causes of the weak biological response but strong SST cooling in the east region of Taiwan.

2 Data and methods

2.1 Data

The typhoon track data used in this study are available from the Unisys Weather website (http://weather.unisys.com/hurricane/w_pacific/), and are based on the hurricane-track data issued by the Joint Typhoon Warning Center (JTWC). The data include the maximum sustained surface wind speed, the location of the hurricane center, and the central pressure at 6-h intervals. The translation speed of the hurricane was subsequently estimated based on the 6-h position of its center in this analysis.

The SST data used are the daily global high-resolution SST (GHRSST) Level 4 (L4) product (http://data.nodc.noaa.gov/ghrsst), which is Advanced Very High Resolution Radiometer (AVHRR) and Advanced Microwave Scanning Radiometer-Earth Observing System (AMSR-E) optimally interpolated (OI) SST with a spatial resolution of 25 km. The merged 8-day averaged Chl-*a* concentration data (Level 3), with a spatial resolution of 9 km, are obtained from both Moderate Resolution Imaging Spectroradiometer (MODIS) and Sea-viewing Wide Field-of-view (SeaWiFS), available from the National Aeronautics and Space Administration (NASA) Goddard Space Flight Center's Ocean Data Processing System. Ocean surface wind data are derived from spatial blending of high-resolution satellite data [Seawinds instrument on the Quick Scatterometer (QuikSCAT)] and National Center for Environmental Prediction (NCEP) reanalyses, which produces high temporal (6-h) and spatial ($0.5° \times 0.5°$) resolution datasets of wind vector components (U and V). Sea surface height anomaly (SSHA) and absolute geostrophic velocity data are obtained from Archiving, Validation and Interpretation of Satellite Oceanographic data (AVISO). This dataset has a temporal resolution of 7-day and a spatial resolution of $1/3° \times 1/3°$. The climatological sea temperature, and nitrate and phosphate mean concentration data are obtained from the World Ocean Atlas 2009 (WOA09). In situ temperature and salinity profiles are from Argo data of the Global Ocean Data Assimilation Experiment (GODAE; http://www.usgodae.org/ftp/outgoing/argo/).

2.2 Methods

Ekman pumping velocity (EPV) is an important index of vertical upwelling movements in the upper ocean. EPV is estimated using wind data, as follows [27]:

$$\mathrm{EPV} = C\mathrm{url}\left(\frac{\vec{\tau}}{\rho f}\right). \tag{1}$$

The wind stress $\vec{\tau}$ is calculated with the following bulk formula:

$$\vec{\tau} = \rho_{\mathrm{a}} C_{\mathrm{d}} |\vec{U}| \vec{U}, \tag{2}$$

where ρ_{a} is the air density (1.29 kg/m^3), ρ is the sea water density (1,020 kg/m^3), f is the Coriolis parameter, U is the wind speed at 10 m, and C_{d} is a wind-speed limited drag coefficient that fits data for low, moderate [28], and high wind speeds [29], as follows:

$$\begin{aligned} C_{\mathrm{d}} \times 10^3 &= 1.2,\ |U| \le 11\,\mathrm{m/s} \\ &= 0.49 + 0.065|U|,\ 11 \le |U| \le 19\,\mathrm{m/s} \\ &= 1.364 + 0.0234|U| - 0.00023158|U|^2,\ 19 \le |U| \le 100\,\mathrm{m/s}. \end{aligned} \tag{3}$$

The mixed layer depth (MLD, m) is defined as the first depth where T is 1.0 °C lower than the temperature of the first observation depth [30]; it is usually about 5 m for the

Argo data. Mixed layer temperature (MLT) and mixed layer salinity (MLS) are the mean temperature and salinity in the mixed layer, respectively.

3 Results

Typhoon Haitang was the first Category 5 super typhoon (Saffir–Simpson scale) of the 2005 season to make landfall in Taiwan and mainland China; it formed at 21.9°N, 154.9°E on July 10. Figure 1 displays its track. It moved northwestward and strengthened into a typhoon on July 13. By July 16 the storm continued tracking west and Haitang strengthened into a Category 5 super typhoon. Influenced by the easterly wind in the south of the subtropical high, the storm direction switched from a south-westerly to a north-westerly direction. On July 17 it weakened to a Category 4 typhoon as it continued its westward movement. Haitang made landfall near Hualien, Taiwan at 00:00 UTC on July 18. It then struck the regions near the midline of Taiwan Strait before turning northwards. Weakening to a tropical storm as it entered the southern East China Sea, Haitang made landfall for the second time near Lianjiang, China at 12:00 UTC on July 19. It rapidly lost its strength and dissipated when it moved over land.

3.1 Surface response to Typhoon Haitang

This study analyses GHRSST L4 SST data. This dataset is a merged product of AVHRR and AMSR-E satellite data. The SST cold patch is usually a pronounced feature of a moving typhoon, which is biased to the right side of the typhoon track in the Northern Hemisphere (from the direction of the typhoon motion). This rightward bias of cooling has been attributed to the asymmetric wind field induced by the translation speed of the typhoon, and also to the "resonance" effects between winds and ocean currents in the intense wind region to the right of the track [4]. Because TC winds rotate in the same direction as inertial currents (to the right of the track in the Northern Hemisphere), this can increase the energy transferred to the currents. SSTs were greater than 30 °C over the majority of the study region before Haitang formed. A previous study has shown that successive SST cooling was found in response to the passage of Haitang between July 11 and July 18 [17]. Of the four regions [17], the decrease in SST in the region to the east of Taiwan (122.5°–128.5°E, 20.5°–24.5°N) was most significant, where SST cooling was evident for a period of 2–3 days. After Haitang reached the northeast of Taiwan (121°–124°E, 25.5°–27.5°N), an additional cold patch was identifiable using AVHRR and AMSR-E data [16]. Due to the different sources of the datasets, there is a slight difference in the absolute magnitude of SST and the position of its cooling. In order to facilitate comparison, the region to the northeast of Taiwan is defined as region A and the region east of Taiwan as region B. The exact positions of these regions are indicated by green rectangles in Fig. 1.

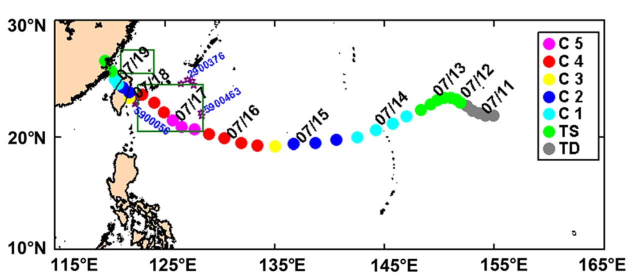

Fig. 1 Study area (*green box*) and track of Typhoon Haitang. *Circles* indicate the typhoon center every 6 h. *Purple pentagrams* indicate the position of Argo floats

The sequential images of SST from July 19 to July 21 are shown in Fig. 2a. In region A the minimum value of SST is 22.93 °C on July 20, and for region B it is 23.88 °C on July 19. The mean SST cooling compared with the pre-typhoon condition is around −2 °C for these two regions. The inverse correlation between SST cooling and Chl-*a* enhancement has been widely documented [1, 9, 25, 26]. The 8-day averaged Chl-*a* images in Fig. 2b suggest a considerable enhancement of Chl-*a* concentration in region A, as would be expected. The mean concentration of Chl-*a* in region A increases dramatically between July 19 and July 26, from the pre-typhoon level of 0.275 to 1.038 mg/m^3. The concentration of Chl-*a* in region B, in contrast, displays no obvious increase (with only an increase of 0.016 mg/m^3 compared with the pre-typhoon level). The hypothesis that greater SST cooling is associated with significant Chl-*a* enhancement is therefore invalid for region B.

3.2 Subsurface response to Typhoon Haitang

Because Argo float data are limited spatially and temporally, just three Argo floats in close proximity to region B are chosen to investigate the subsurface response to Haitang. The vertical profiles of temperature and salinity from the floats during the typhoon are shown in Fig. 3. MLD, MLT, and MLS are also calculated (Table 1). Float D5900463 is located to the right side of the track, where the MLD is 42 m deeper than the pre-typhoon depth. This is caused by enhanced mixing processes due to a combination of surface wind stress and cooling [31], and vertical current shear at the base of the mixed layer [4]. Meanwhile, the MLT decreases by about 2 °C, and MLS increases by 0.04 psu. For float R2900376, the data show that the MLD is 43 m deeper on July 18 compared with the pre-typhoon

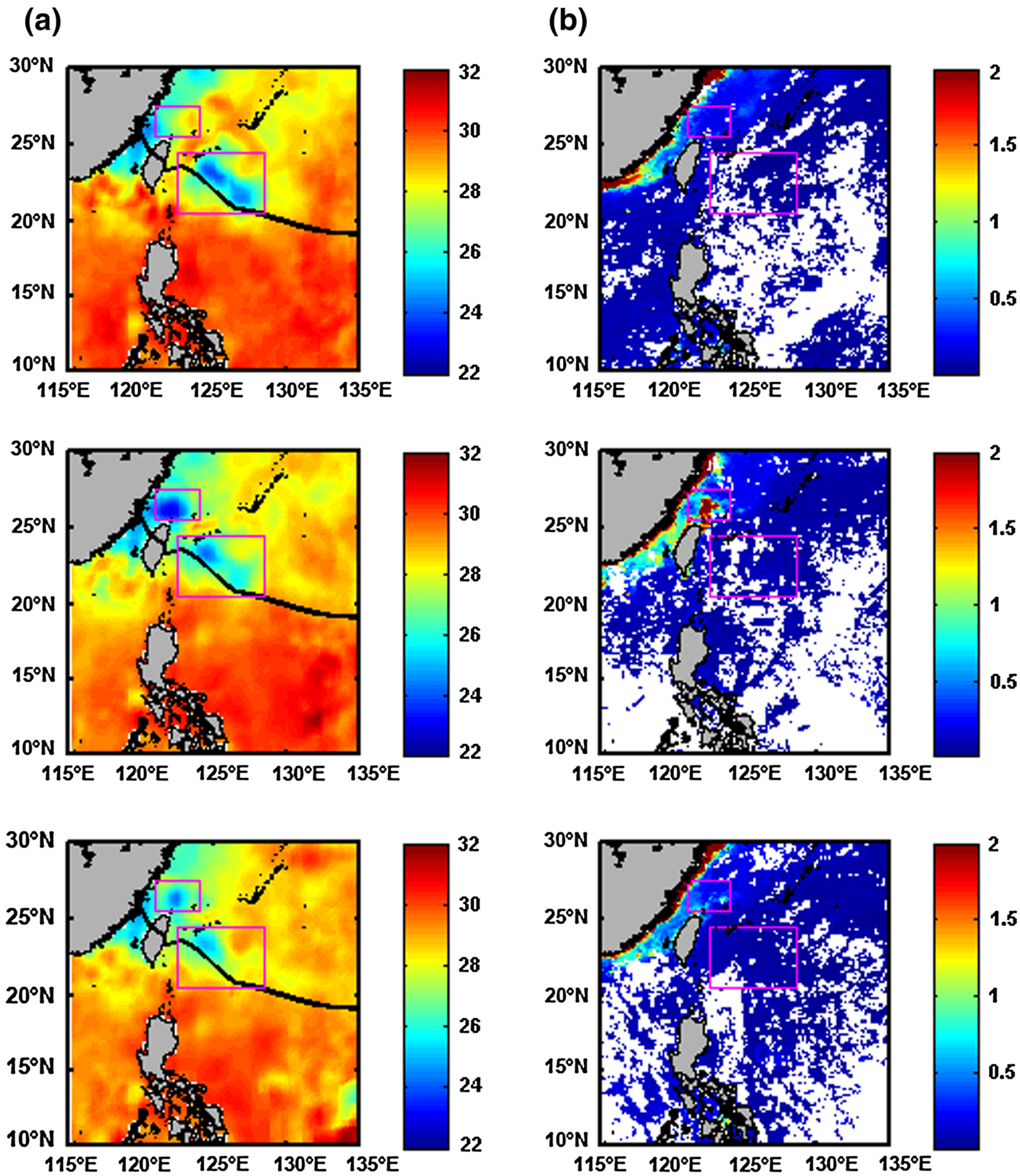

Fig. 2 SST (°C) images **a** from July 19 to July 21 and 8-day averaged Chlorophyll-*a* (Chl-*a*) concentration (mg/m^3); **b** for the periods July 11–18, July 19–26, July 27 to August 3, respectively

conditions on July 14, while MLT decreases by 1.5 °C on July 24, which is a slightly smaller decrease than that recorded by D5900463. Of the three Argo floats, R5900056 is the only one located to the left of the typhoon track, but is still situated within close proximity to the track. At this location the MLD is 27 m deeper on July 18, and the decrease in MLT lags the deepening of the MLD by 4 days.

The role of mixing and upwelling is examined using the Argo profiles (Fig. 3). Temperature drops in the upper 40 m, but increases below 40 m at D5900463, which emphasizes the importance of the mixing process at this location. Salinity increases in the upper 40 m and below 100 m, but decreases between these two layers as a result of mixing. Salinity also decreases at the bottom of the mixed layer due to upwelling of saline deep water. For float R2900376, temperature decreases above 60 m, and increases below 60 m. However, the magnitude of change in salinity is much smaller in the layer below 60 m for R2900376 compared with D5900463, suggesting that upwelling makes little contribution at this location and that mixing is the dominant process. Temperature drops throughout almost the entire water column for R5900056. Salinity decreases above 100 m at this location because of rainfall, and increases slightly below 80 m, which implies

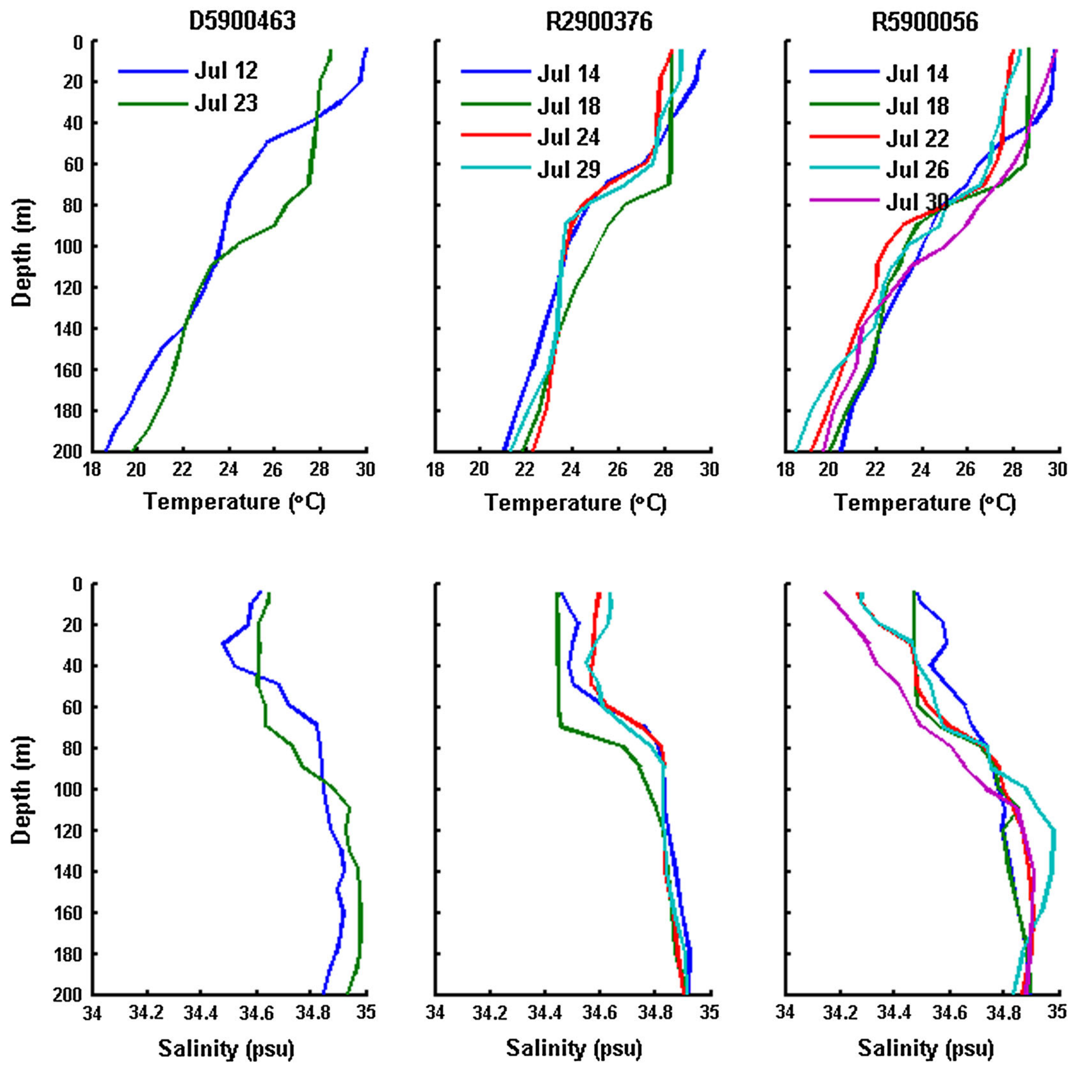

Fig. 3 Vertical profiles of temperature and salinity measured by Argo floats (locations are marked by *purple pentagrams* in Fig. 1)

that upwelling is a key process in this area. In region B the mixing process is shown to be dominant overall.

4 Discussion

Although the magnitude of SST cooling in region A and B is similar, the mechanisms are different. Ekman pumping, which is forced by the spatially inhomogeneous wind stress field, is a useful oceanographic measure of the direct effect of wind stresses on the upper layer of the ocean. Figure 4 shows comparison maps for wind speed, SST, and EPV for the period July 11–31 for the two regions. These show high EPV values prior to the SST cooling in region A, indicating strong upwelling in this region that induces the cooling of SST. The mixing in region A is also important, because the entrainment/mixing accounts for 75 %–90 % of the SST drop in the wake of a TC [4, 6, 7].

Negative sea surface height anomaly (SSHA) features are regions where sea surface height shoals relative to the climatology [32–34]. The SSHA maps (Fig. 5a) show evidence of two cold eddies in region B where the water column is denser than normal. The eddies exist in this region throughout the passage of typhoon Haitang. Mesoscale eddies are a material source for the formation of an extreme cooling center. The strong wind-driven turbulent mixing resulting from wind stress is conducive to the upwelling of cold water. Although the mean wind speed is nearly 20 m/s and the maximum EPV in region B can reach 103.51×10^{-6} m/s, the regional mean EPV is negative. The high translation speed of the typhoon (nearly 5 m/s) around region B means there is insufficient time for Haitang to bring cold water up from the lower layer. Nevertheless, a near-inertial current to the right side of the TC can be excited due to shear-induced entrainment of the mixed layer [4]. Ekman pumping, therefore, plays an important role in relation to the drop in SST and should not be disregarded when investigating typhoon processes [19], although it makes less of a contribution than other processes. The vertical profiles of temperature and salinity (Fig. 3) also show that mixing is dominant in region B, which therefore contributes to SST cooling. The significant SST cooling in region B can be attributed to the mixing processes, combined with the cold eddy.

The causes of the different biological responses in regions A and B are now examined. The enhancement of Chl-*a* is commonly influenced by the upwelling of nutrients from below the euphotic layer, which supplies the nutrients required for phytoplankton growth [26, 35]. Chang et al. [16] suggested that the enhancement of Chl-*a* in region A is related to the high velocity of Ekman Pumping, and that the wind-driven Kuroshio moves more shoreward, increasing its intrusion onto the shelf-break.

Table 1 Observations by Argo floats

Argo	Date (2005)	Position	MLD (m)	MLT (°C)	MLS (psu)
D5900463	Jul 12	128.404°E/21.832°N	27.703	29.849	34.585
	Jul 23	128.356°E/22.079°N	69.762	27.891	34.622
R2900376	Jul 14	126.466°E/24.605°N	30.962	29.311	34.486
	Jul 18	127.049°E/24.961°N	73.856	28.241	34.440
	Jul 24	127.543°E/24.795°N	57.016	27.864	34.577
	Jul 29	127.692°E/24.456°N	44.403	28.379	34.603
R5900056	Jul 14	122.430°E/23.108°N	40.466	29.516	34.532
	Jul 18	122.300°E/22.847°N	67.576	28.604	34.474
	Jul 22	122.150°E/23.218°N	64.063	27.619	34.400
	Jul 26	122.323°E/23.412°N	42.645	27.828	34.367
	Jul 30	122.247°E/23.495°N	34.145	29.479	34.218

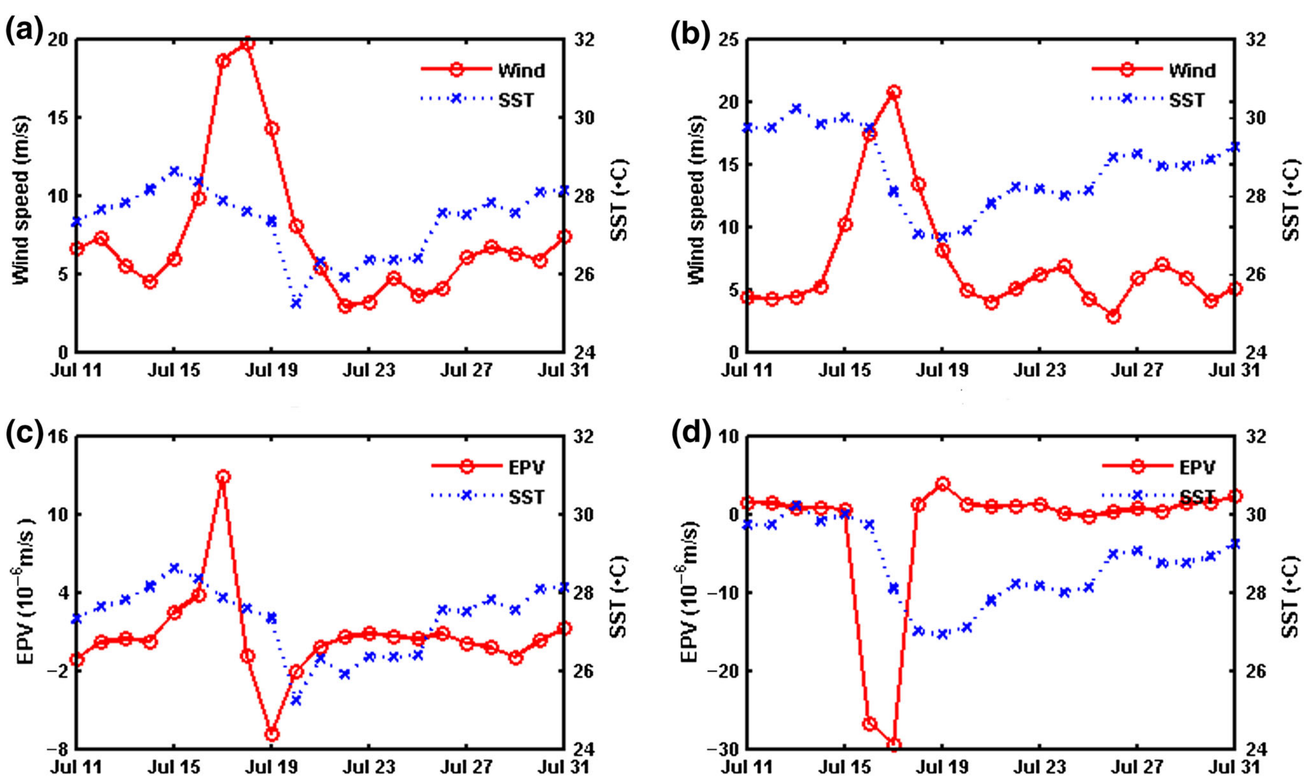

Fig. 4 Time series of mean wind speed (m/s) and mean SST (°C) (**a**, **b**), and mean EPV ($\times 10^{-6}$ m/s) and mean SST (°C) (**c**, **d**) between July 11 and July 31 for regions A (**a**, **c**) and B (**b**, **d**)

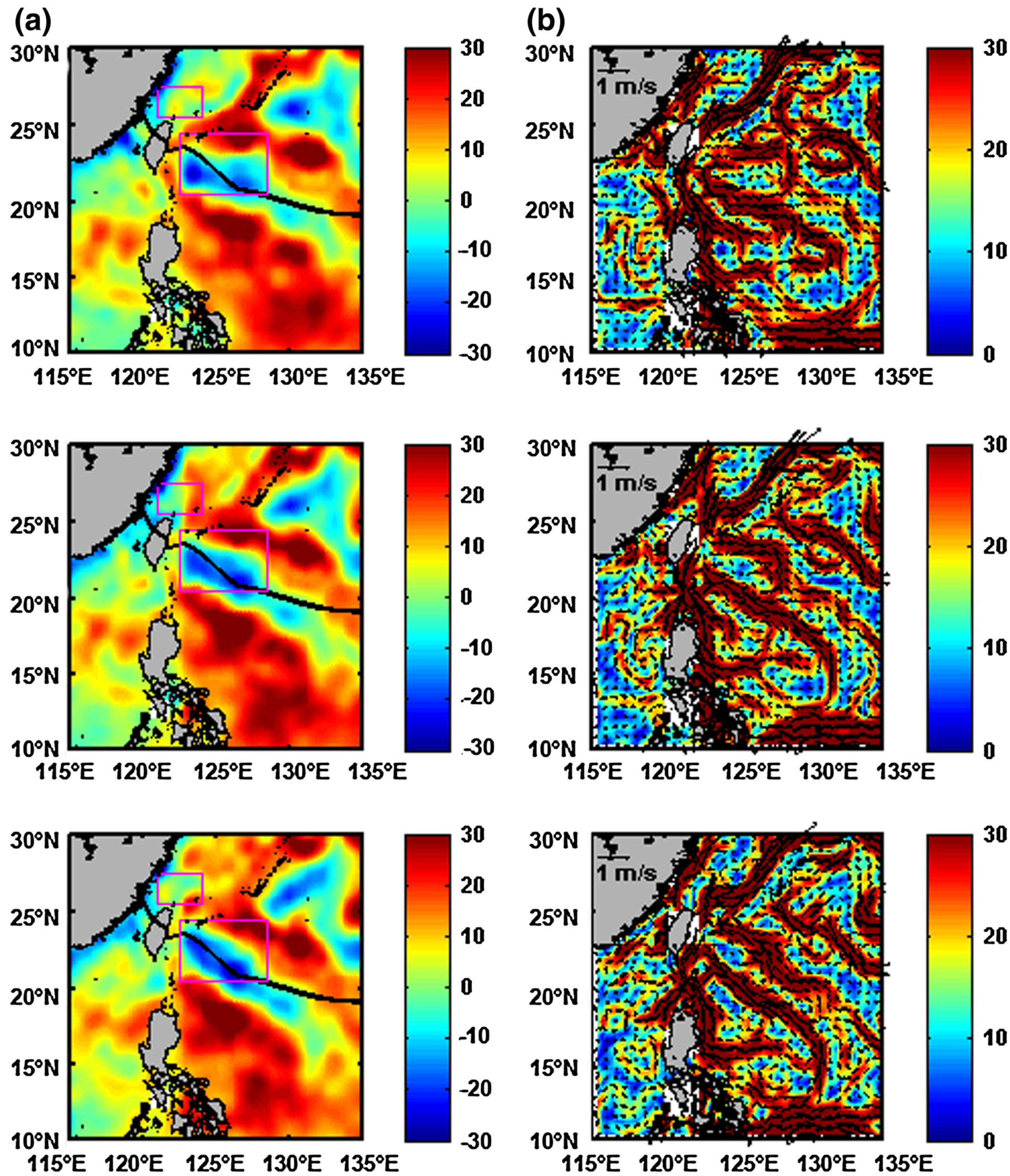

Fig. 5 Maps of SSHA (cm) (**a**) and absolute geostrophic velocities (cm/s) (**b**) derived from AVISO for July 13, July 20, and July 27

Ocean radar data indicate that the Kuroshio axis moved onto the shelf after the passage of Haitang [20]. The present study yields similar results based on SSHA and absolute geostrophic velocity data from AVISO. The images of the absolute geostrophic velocities (Fig. 5b) suggest that the Kuroshio flows north-eastward on July 13, but the pattern alters after the passage of the typhoon, with a northward flow on July 20 and an apparent shift of the axis onto the shelf. The image of SSHA in region A shows a higher pressure gradient on July 20. According to the geostrophic relation, this implies the existence of a strong northward current, which could enhance the Kuroshio and push it east of Taiwan onto the shelf. The Kuroshio contains a maximum nutrient flux core in the middle layer [36]. As the subsurface water moves onto the shelf due to the movement of the Kuroshio axis, vertical flow associated with the horizontal current shear of the Kuroshio triggers the upwelling of subsurface water, which results in Chl-*a* enhancement in region A. The EPV and the intrusion of the Kuroshio onto the shelf-break contribute to the enhancement of Chl-*a* in region A.

The mean Chl-*a* concentration in region A was 0.42 mg/m^3, compared with 0.06 mg/m^3 in July for region B. The depth of the euphotic layer can be calculated with Chl-*a* concentration according to the approach of Morel et al. [37]. The depth of the euphotic layer in regions A and

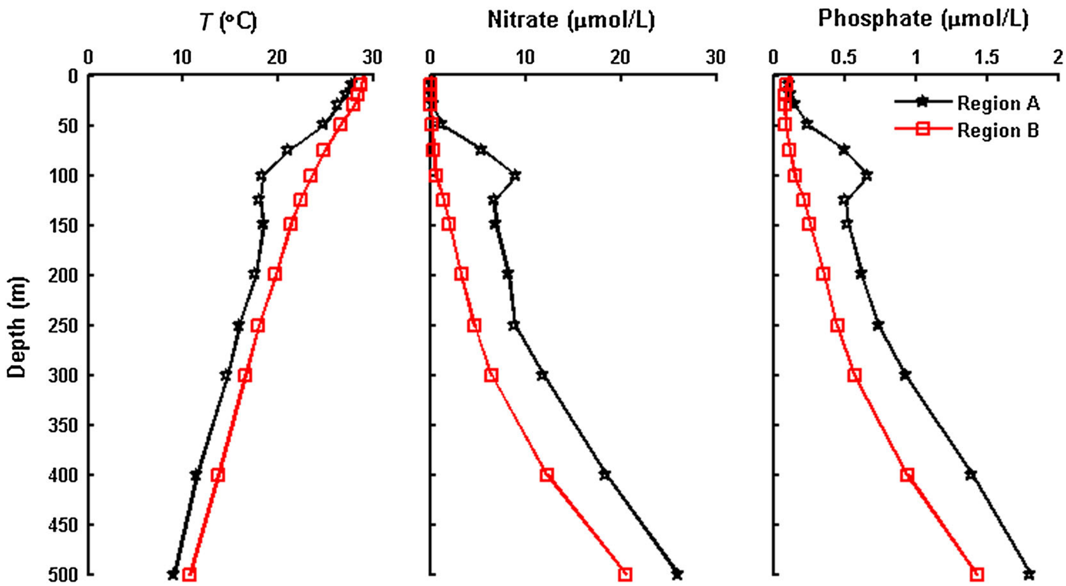

Fig. 6 Vertical distribution of temperature (°C), and nitrate and phosphate climatological mean concentrations (μmol/L) for regions A and B

B was approximately 40 and 100 m, respectively. The vertical distribution of nitrate and phosphate climatological mean concentrations, derived from WOA09, is displayed in Fig. 6. Nutrient concentrations are depleted in the euphotic layer, and gradually increase with depth below 100 m for region B. While for region A the nutrient concentrations began to increase at about 40 m. The nutricline is deeper in region B than that in region A, and temperature gradually decreases with depth below the bottom of the mixed layer. Previous results suggest that upwelling in region B is less important, with mixing being the dominant process. It is unlikely that entrainment alone would change the vertical Chl-*a* average, especially when the MLD is significantly shallower than the euphotic layer depth. Because photosynthesis is dependent upon both nutrient concentration and light intensity, Chl-*a* concentration is unlikely to increase in region B where the rich nutrients are unable to be transported to the euphotic layer because of the shallow mixed layer. However, the mixing process could transport the colder water toward the surface, which would reduce SST.

In a numerical simulation of the western subtropical North Pacific, Shibano et al. [38] showed that when upwelling is less important and the MLD is shallower than the nutricline, then SST would decrease but the surface nutrient concentration would be only weakly affected. In a cyclonic eddy, upwelling can bring cold nutrient-rich water up from the deep layer to the euphotic layer, and thus enhance the nutrient concentration. The water column is strongly stratified during the summer, but the cold subsurface water and enhanced nutrient concentrations are not distinct in regions of cyclonic circulation. Therefore, no significant enhancement of Chl-*a* is seen in region B, but strong SST cooling occurs.

5 Conclusions

The responses of the upper ocean to Typhoon Haitang are investigated using Argo floats and multiplatform satellite data. We identify two extreme cooling regions (region A and B). While the magnitude of SST cooling at regions A and B is similar, the biological response differs. In region A, where significant blooming occurs, Ekman pumping and movement of the Kuroshio contribute to the Chl-*a* enhancement. In contrast, EPV has little influence on cooling in region B because of the relatively high translation speed of the typhoon, which gives insufficient time for Haitang to induce cold water upwelling or enhance Chl-*a*. The pre-typhoon ocean environment (cold eddies) provides a material source for the formation of an extreme cooling center. Vertical mixing and the cold eddy are primarily responsible for the SST cooling at region B. As upwelling is less important in this region, and because the MLD is shallower than the nutricline, SST decreases but the surface nutrient concentration remains only weakly affected. This is evidenced by SST gradually decreasing with depth below the bottom of the mixed layer, whereas nutrient concentration is more uniformly depleted down to a depth of 100 m.

In this study we analyze satellite and Argo data, but a limiting factor is the scarcity of observation data. Model simulations offer a complementary method for studying the mechanisms of response to a typhoon, and for investigating the interaction with wind fields, mesoscale eddies, ocean currents and waves.

Acknowledgments We thank JTWC for providing typhoon track data, NASA's Ocean Color Working Group for providing merged MODIS and SeaWiFS data, NODC for GHRSST data, UCAR for QSCAT/NCEP Blended Ocean Wind data, AVISO for SSHA data and geostrophic current data, and GODAE for ARGO float profiles. This work was supported by the National Natural Science Foundation of China (40976011), the National Basic Research Program of China (2013CB430300), and the Public Science and Technology Research Funds Projects of Ocean (201105018).

References

1. Lin I, Liu WT, Wu C-C et al (2003) New evidence for enhanced ocean primary production triggered by tropical cyclone. Geophys Res Lett 30:1781. doi:10.1029/2003GL017141
2. Shang S, Li L, Sun F et al (2008) Changes of temperature and bio-optical properties in the South China Sea in response to Typhoon Lingling, 2001. J Geophys Res 35:L10602. doi:10.1029/2008GL033502
3. Shan HX, Guan YP, Wang DX et al (2012) Responses of equatorial ocean to rare typhoon Vamei. J Tropical Oceanogr 31:28–34 (in Chinese)
4. Price JF (1981) Upper ocean response to a hurricane. J Phys Oceanogr 11:153–175
5. Price JF, Sanford TB, Forristall GZ (1994) Forced stage response to a moving hurricane. J Phys Oceanogr 24:233–260
6. Huang P, Sanford TB, Imberger J (2009) Heat and turbulent kinetic energy budgets for surface layer cooling induced by the passage of Hurricane Frances (2004). J Geophys Res 114:C12023. doi:10.1029/2009JC005603
7. Jacob SD, Shay LK, Marianoand AJ et al (2000) The 3D oceanic mixed layer response to Hurricane Gilbert. J Phys Oceanogr 30:1407–1429
8. Lin I-I, Pun I-F, Wu C-C (2009) Upper-ocean thermal structure and the western North Pacific Category 5 Typhoons. Part II: dependence on translation speed. Mon Weather Rev 137:3744–3757
9. Babin SM, Carton JA, Dickey TD et al (2004) Satellite evidence of hurricane-induced phytoplankton blooms in an oceanic desert. J Geophys Res 109:C03043. doi:10.1029/2003JC001938
10. Wu C-R, Chang Y-L, Oey L-Y et al (2008) Air-sea interaction between tropical cyclone Nari and Kuroshio. Geophys Res Lett 35:L12605. doi:10.1029/2008GL033942
11. Tsai Y, Chern CS, Wang J (2008) The upper ocean response to a moving typhoon. J Oceanogr 64:115130
12. Oey L-Y, Ezer T, Wang DP et al (2007) Hurricane-induced motions and interaction with ocean currents. Cont Shelf Res 27:1249–1263
13. Sheng J, Wang L, Andréfouët S et al (2007) Upper ocean response of the Mesoamerican Barrier Reef System to Hurricane Mitch and coastal freshwater inputs: a study using Sea-viewing Wide Field-of-view Sensor (SeaWiFS) ocean color data and a nested-grid ocean circulation model. J Geophys Res 112:C07016. doi:10.1029/2006JC003900
14. Liu XM, Wang M, Shi W (2009) A study of a Hurricane Katrina-induced phytoplankton bloom using satellite observations and model simulations. J Geophys Res 114:C03023. doi:10.1029/2008JC004934
15. Nam SH, Kim D-J, Moon WM (2012) Observed impact of mesoscale circulation on oceanic response to Typhoon Man-Yi 2007. Ocean Dyn 62:1–12
16. Chang Y, Liao H-T, Lee M-A et al (2008) Multisatellite observation on upwelling after the passage of Typhoon Hai-Tang in the southern East China Sea. Geophys Res Lett 35:L03612. doi:10.1029/2007GL032858
17. Zheng Z-W, Ho C-R, Kuo N-J (2008) Importance of pre-existing oceanic conditions to upper ocean response induced by Super Typhoon Hai-Tang. Geophys Res Lett 35:L20603. doi:10.1029/2008GL035524
18. Ho C-R, Zheng Q, Zheng Z-W et al (2009) Reply to comment by A. Wada et al. on "Importance of pre-existing oceanic conditions to upper ocean response induced by Super Typhoon Hai-Tang". Geophys Res Lett 36:L09604. doi:10.1029/2009GL037443
19. Wada A, Sato K, Usui N et al (2009) Comment on "Importance of pre-existing oceanic conditions to upper ocean response induced by Super Typhoon Hai-Tang" by Z.-W. Zheng, C.-R. Ho, and N.-J. Kuo. Geophys Res Lett 36:L09603. doi:10.1029/2008GL036890
20. Morimoto A, Kojima S, Jan S (2009) Movement of the Kuroshio axis to the northeast shelf of Taiwan during typhoon events. Estuar Coast Shelf Sci 82:547–552
21. Wada A, Usui N (2010) Impacts of oceanic preexisting conditions on predictions of Typhoon Hai-Tang in 2005. Adv Meteorol 2010:756071. doi:10.1155/2010/756071
22. Wada A, Kohno N, Kawai Y (2010) Impact of wave–ocean interaction on Typhoon Hai-Tang in 2005. Sci Online Lett Atmos 6A:13–16
23. Zheng Z-W, Ho C-R, Zheng Q et al (2010) Effects of preexisting cyclonic eddies on upper ocean responses to Category 5 typhoons in the western North Pacific. J Geophys Res 115:C09013. doi:10.1029/2009JC005562
24. Chang Y-C, Tseng R-S, Centurioni LR (2010) Typhoon-induced strong surface flows in the Taiwan Strait and Pacific. J Oceanogr 66:175–182
25. Walker ND, Leben RR, Balasubramanian S (2005) Hurricane-forced upwelling and Chlorophyll-*a* enhancement within cold-core cyclones in the Gulf of Mexico. Geophys Res Lett 32:L18610. doi:10.1029/2005GL023716
26. Subrahmanyam B, Rao KH, Rao NS et al (2002) Influence of a tropical cyclone on Chlorophyll-*a* concentration in the Arabian Sea. Geophys Res Lett 29:2065. doi:10.1029/2002GL015892
27. Zhao H, Tang DL (2007) Effect of 1998 El Niño on the distribution of phytoplankton in the South China Sea. J Geophys Res 112:C02017. doi:10.1029/2006JC003536
28. Large WG, Pond S (1981) Open ocean flux measurements in moderate to strong winds. J Phys Oceanogr 11:324–336
29. Powell MD, Vickery PJ, Reinhold TA (2003) Reduced drag coefficient for high wind speeds in tropical cyclones. Nature 422:279–283
30. Kara AB, Rochford PA, Hurlburt HE (2000) An optimal definition for ocean mixed layer depth. Geophys Res Lett 105:16803–16821. doi:10.1029/2000JC900072
31. Elsberry RL, Fraim TS, Trapnell RN Jr (1976) A mixed layer model of the ocean thermal response to hurricanes. J Geophys Res 81:1153–1162. doi:10.1029/JC081i006p01153
32. Lin I-I, Wu C-C, Emanuel KA et al (2005) The interaction of Supertyphoon Maemi (2003) with a Warm Ocean Eddy. Mon Weather Rev 133:2635–2649
33. Scharroo R, Smith WHF, Lillibridge JL (2005) Satellite altimetry and the intensification of Hurricane Katrina. EOS Trans AGU 86:366
34. Pun I-F, Lin I–I, Wu C-R et al (2007) Validation and application of altimetry-derived upper ocean thermal structure in the Western

North Pacific Ocean for Typhoon intensity forecast. IEEE Trans Geosci Remote Sens 45:1616–1630

35. Shi W, Wang M (2007) Observations of a Hurricane Katrina induced phytoplankton bloom in the Gulf of Mexico. Geophys Res Lett 34:L11607. doi:10.1029/2007GL029724
36. Guo X, Zhu X-H, Wu Q-S et al (2012) The Kuroshio nutrient stream and its temporal variation in the East China Sea. J Geophys Res 117:C01026. doi:10.1029/2011JC007292
37. Morel A, Huot Y, Gentili B et al (2007) Examining the consistency of products derived from various ocean color sensors in open ocean (Case 1) waters in the perspective of a multi-sensor approach. Remote Sens Environ 111:69–88
38. Shibano R, Yamanaka Y, Okada N et al (2011) Responses of marine ecosystem to typhoon passage s in the western subtropical North Pacific. Geophys Res Lett 38:L18608. doi:10.1029/2011GL048717